ARTICLE   OPEN

Check for updates

Quantifying quantum coherence of multiple-charge states in tunable Josephson junctions

Jiangbo He [1,10], Dong Pan [2,10], Mingli Liu[1,3], Zhaozheng Lyu [1,4], Zhongmou Jia[1,3], Guang Yang[1], Shang Zhu[1,3], Guangtong Liu [1,4,5], Jie Shen [1,5], Sergey N. Shevchenko[6], Franco Nori [7,8,9 ✉], Jianhua Zhao [2 ✉], Li Lu [1,3,4,5 ✉] and Fanming Qu [1,3,4,5 ✉]

Coherence and tunneling play central roles in quantum phenomena. In a tunneling event, the time that a particle spends inside the barrier has been fiercely debated. This problem becomes more complex when tunneling repeatedly occurs back and forth, and when involving many particles. Here we report the measurement of the coherence time of various charge states tunneling in a nanowire-based tunable Josephson junction; including single charges, multiple charges, and Cooper pairs. We studied all the charge tunneling processes using Landau-Zener-Stückelberg-Majorana (LZSM) interferometry, and observed high-quality interference patterns under a microwave drive. In particular, the coherence time of the charge states tunneling back and forth was extracted from the interference fringes in Fourier space. In addition, our measurements show the break-up of Cooper pairs, from a macroscopic quantum coherent state to individual particle states. Besides the fundamental research interest, our results also establish LZSM interferometry as a powerful technique to explore the coherence time of charges in hybrid devices.

INTRODUCTION

In a quantum tunneling event, a fundamental open question is the time spent by the particle(s) inside the barrier[1–6]. Another unsolved issue is the coherence time[7] of the back-and-forth tunneling process through the barrier, especially for multi-particles. Josephson junctions (JJs) provide a platform for studying tunneling processes of various charges; including single charges, coherent multiple charges, and Cooper pairs[8–10]. When a voltage is applied to a JJ, the well-known multiple Andreev reflections (MARs) provide a mechanism for the coherent transfer of multiple charges, up to infinity[11]. At the gap edge, the tunneling of single charges (Giaever tunneling) contributes to a coherence peak[12]. In addition, a JJ usually inherits the macroscopic quantum coherent nature of the superconductor. However, for an ultra-small JJ with a low capacitance and a weak Josephson coupling, the phase fluctuates significantly and is no longer a good quantum number, leading to a loss of macroscopic quantum coherence of Cooper pairs, regressing to individual particle states[9,12,13]. Accordingly, the Shapiro-step picture breaks down under microwave driving[14–16]. Therefore, a tunable JJ can serve as a unique platform for studying the coherence of tunneling processes of many charges, and for monitoring the disappearance and establishment of macroscopic quantum coherence of the Cooper pairs.

In recent years, scanning-tunneling-microscope (STM) experiments utilizing a superconducting tip have been used to distinguish the tunneling processes of the charges under microwave drive. The results were interpreted based on the Tien-Gordon theory and/or the microwave-assisted MAR model[13,17–21]. But the coherence time of various charges that tunnel back and forth through the barrier has not yet been examined. A systematic investigation of the onset and disappearance of macroscopic quantum coherence of the Cooper pairs in an ultra-small JJ is missing.

Interferometry can probe the coherence times of quantum states. Recently, Landau-Zener-Stückelberg-Majorana (LZSM) interferometry[22–24] has gained great success as a tool to diagnose the physical parameters and also to realize fast coherent manipulation of isolated qubits[25–32]. In this work, we implemented LZSM interferometry in a gate-tunable nanowire-based JJ, which is an open system (i.e., directly connected to the measurement circuit), in contrast to the generally isolated qubits. We constructed the JJ down to the single ballistic-channel limit, allowing us to resolve LZSM interference for single charges, multiple charges, and Cooper pairs—in the weak coupling regime and under the drive of microwaves. Through analyzing the interference fringes in the two-dimensional (2D) Fourier space, we extracted the coherence times of all these charge states that tunnel back and forth through the junction. We further uncovered the loss of macroscopic quantum coherence of the Cooper pairs in the JJs.

The LZSM model assumes a system with a discrete energy spectrum whose temporal modulation produces interlevel transitions. In this sense, it allows the description of the tunneling between states as soon as the relevant states are identified. This approach allows us to consider various-charge states in one context, namely, we will consider within this model the tunneling of Cooper-pairs, 2- and 3-charges through MARs, and single charges. These three different phenomena were previously well studied[18,33–38] using more microscopic models, providing various derivations and results. The LZSM model allows considering the tunneling of various charges from a different, but complementary,

[1]Beijing National Laboratory for Condensed Matter Physics, Institute of Physics, Chinese Academy of Sciences, Beijing 100190, China. [2]State Key Laboratory of Superlattices and Microstructures, Institute of Semiconductors, Chinese Academy of Sciences, P.O. Box 912, Beijing 100083, China. [3]School of Physical Sciences, University of Chinese Academy of Sciences, Beijing 100049, China. [4]Hefei National Laboratory, Hefei 230088, China. [5]Songshan Lake Materials Laboratory, Dongguan 523808, China. [6]B. Verkin Institute for Low Temperature Physics and Engineering, Kharkiv 61103, Ukraine. [7]Theoretical Quantum Physics Laboratory, Cluster for Pioneering Research, RIKEN, Wakoshi, Saitama 351-0198, Japan. [8]Quantum Computing Center, RIKEN, Wakoshi, Saitama 351-0198, Japan. [9]Physics Department, The University of Michigan, Ann Arbor, MI 48109-1040, USA. [10]These authors contributed equally: Jiangbo He, Dong Pan. ✉email: fnori@riken.jp; jhzhao@semi.ac.cn; lilu@iphy.ac.cn; fanmingqu@iphy.ac.cn
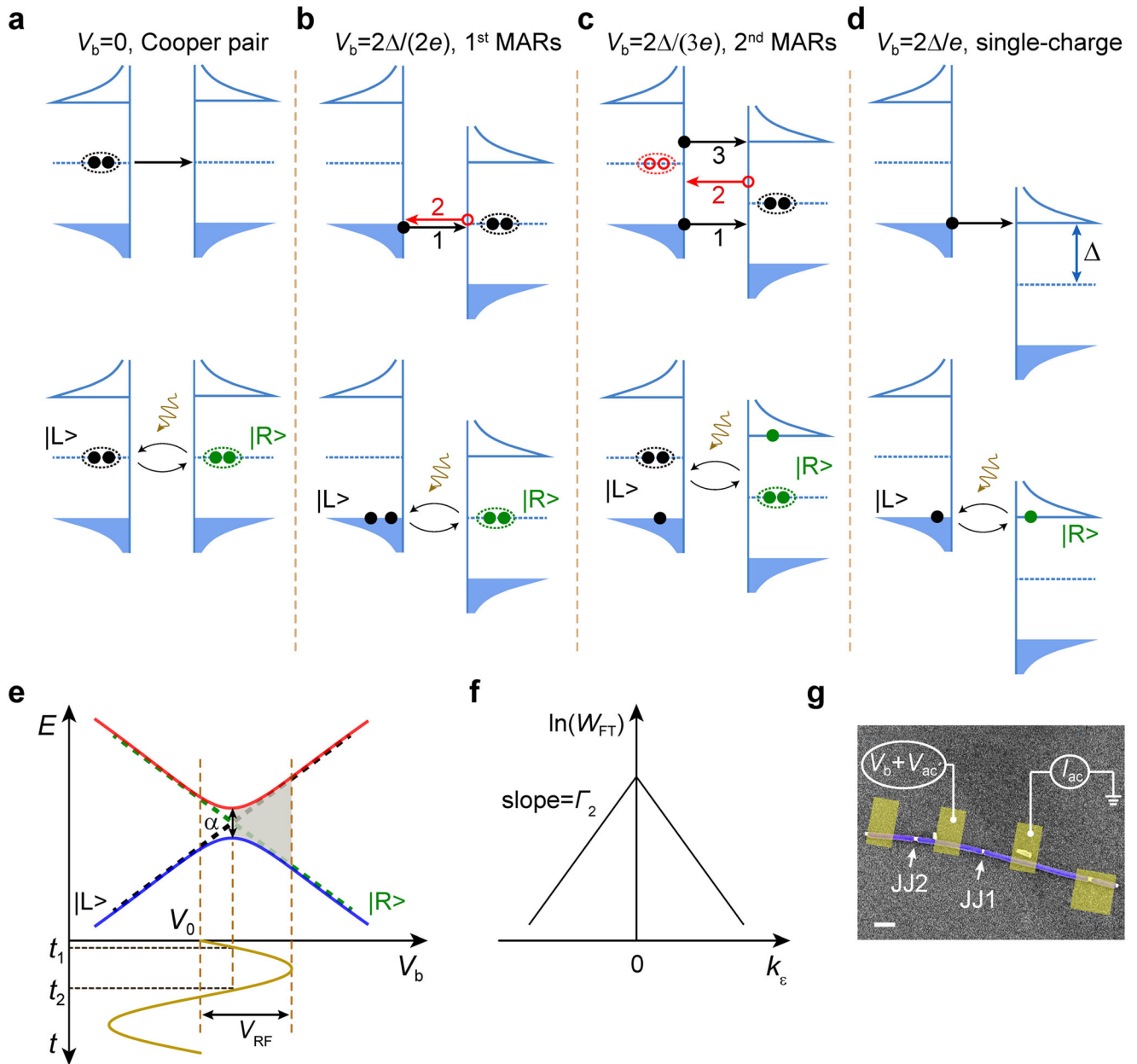
Fig. 1 Illustration of LZSM interference in a Josephson junction. a–d Charge tunneling at typical bias voltages V_b. The arrows in (**b**) and (**c**) indicate successive Andreev reflections. |L> and |R> represent the two effective states where charges tunnel back and forth under a microwave drive. **e** The dashed lines show the adiabatic energy levels for the states |L> and |R>; the solid blue and red curves show the energy levels when taking tunneling into account. A microwave (brown) drives the system through the anti-crossing at the time t_1 where LZSM transitions occur, and back to the anti-crossing at time t_2, where the two trajectories interfere. **f** Linear dependence of $\ln(W_{FT})$ on $|k_\varepsilon|$, whose slope is $\pm\Gamma_2$. **g** The nanowire (white) contains JJ1 and JJ2. Aluminum is shown in violet, and the yellow rectangles denote post-fabricated Ti/Au contacts. Scale bar: 200 nm.

perspective. Moreover, the involvement of coherence and decoherence is enabled in the quantum interference process.

RESULTS AND DISCUSSION
LZSM interferometry
Before presenting the experimental results, we first interpret the physical picture of LZSM interference in an ultra-small JJ. Phase fluctuations lead to the loss of macroscopic quantum coherence and Cooper pair tunneling as individual microscopic particles[9,12,13] (Fig. 1a). MARs enable a coherent transfer of 2-charges through a 1st-order reflection (Fig. 1b) and 3-charges through a 2nd-order

reflection (Fig. 1c). Single charge tunneling is activated when the voltage reaches $V_b = 2\Delta/e$ (Δ is the superconducting gap and e is the elementary charge) (Fig. 1d). However, to enable LZSM interferometry, two coupled energy levels plus a fast ac drive are required[39]. For a JJ, an open system, we argue that thanks to the singularities of the BCS single particle density of states and the Cooper pair condensate, the effective two levels can be mapped to the charges being at the left and the right sides of the junction, respectively. These two states, |L> and |R>, are shown in the bottom row of Fig. 1a–d. The charges can tunnel between these two states under a microwave drive.

Figure 1e illustrates LZSM interference. When a harmonic drive $V_{RF} \cos(\omega t)$ ($\omega = 2\pi f$, with f being the frequency of the microwave)

is applied, the Hamiltonian of the system can be expressed as $H = -\frac{\hbar}{2}\begin{pmatrix} \beta(t) & \alpha \\ \alpha & -\beta(t) \end{pmatrix}$, where $\beta(t) = \varepsilon - A\cos(\omega t)$, $\varepsilon = meV_0$ is the detuning energy, V_0 is the voltage relative to the anti-crossing point (see Fig. 1e), $A = meV_{RF}$, $m = 1, 2, 3\dots$ represents the number of charges in an elementary tunneling event, and $\alpha/2$ is the coupling strength of the JJ. The two-level system as shown in Fig. 1e can be directly obtained after a rotation of the Hamiltonian. The two states |L> (black dashed line) and |R> (green dashed line) anti-cross, with a minimal distance α, which is twice the coupling strength. The junction is detuned by V_0 relative to the anti-crossing point, and a harmonic microwave (brown curve) with an amplitude V_{RF} drives the system adiabatically to, and nonadiabatically through, the anti-crossing at time $t = t_1$, with a transition probability of $P_{LZSM} = \exp(-\pi\alpha^2/2v\hbar)$, where v is the sweeping velocity. The two trajectories accumulate a phase difference (the shaded area) until $t = t_2$, when the system is brought back to the anti-crossing, where LZSM interference occurs.

The continuous microwave drive sustains the interference of the alternating tunneling until the charges lose coherence. To incorporate the environmental decoherence, classical noise can be introduced to the microwave drive, and a white noise model is employed under perturbation, to obtain the rate of transitions between |L> and |R>[40,41]

$$W(\varepsilon, A) = \frac{\alpha^2}{2}\sum_{n=-\infty}^{+\infty}\frac{\Gamma_2 J_n^2\left(\frac{A}{\hbar\omega}\right)}{(\varepsilon - n\hbar\omega)^2 + \hbar^2\Gamma_2^2}, \quad (1)$$

where $\Gamma_2 = 1/T_2$ is the decoherence rate, $n = \pm 1, \pm 2\dots$ denotes the satellite replicas of the $n = 0$ Lorentzian-shaped peaks, J_n is the Bessel function of the first kind. Evidently, the observability (broadening) of the interference fringes depends on the competition between ω and Γ_2.

The coherence time $T_2 = 1/\Gamma_2$ can be conveniently characterized in Fourier space by inverting the energy variable to the time variable. A 2D Fourier transform (2D FT) of $W(\varepsilon, A)$ yields[40]

$$W_{FT}(k_A, k_\varepsilon) = \frac{\alpha^2 \omega e^{-\Gamma_2|k_\varepsilon|}}{2\sqrt{\frac{4}{\omega^2}\sin^2\left(\frac{1}{2}\omega k_\varepsilon\right) - k_A^2}} \quad (2)$$

for $|k_A| < \frac{2}{\omega}\left|\sin\left(\frac{1}{2}\omega k_\varepsilon\right)\right|$ and zero otherwise. The reciprocal-space variables k_A and k_ε correspond to the energy variables A and ε, respectively. Therefore, lemon-shaped ovals following the singular boundary $\frac{\omega}{2}k_A = \pm\sin\left(\frac{1}{2}\omega k_\varepsilon\right)$, and an exponential decay on k_ε as $e^{-\Gamma_2|k_\varepsilon|}$, are expected (see Supplementary Note 3). Figure 1f illustrates a linear dependence of $\ln(W_{FT})$ on $|k_\varepsilon|$, whose slope generates the coherence time $T_2 = 1/\Gamma_2$.

Epitaxial nanowire JJs

Next, we present the experimental results. InAs$_{0.92}$Sb$_{0.08}$ nanowires were grown by molecular beam epitaxy, followed by an in situ epitaxy of ~15 nm-thick Al at a low temperature, which guarantees a hard superconducting gap[42,43]. Narrow Al gaps (JJs) were formed naturally during growth due to shadowing between the dense nanowires, eliminating the wet etching process and possible degradations. Figure 1g shows the nanowire possessing two JJs studied in this work, with Al gaps of ~20 nm (JJ1) and ~40 nm (JJ2), respectively. The yellow rectangles show post-fabricated Ti/Au (10/80 nm) contacts. Standard lock-in techniques and a microwave antenna were applied to carry out the transport measurements at ~10 mK. We will focus on JJ1 in the main text and present typical results for JJ2 in Supplementary Notes 7 and 8.

One of the advantages of the nanowire-based JJ is its full gate tunability. By applying a gate voltage V_G (Fig. 2a, b), the JJ could be tuned to the strong coupling regime, the single ballistic-channel limit, and the weak-coupling regime. Figure 2a displays

the correlation between the conductance dI/dV measured at the normal state and the critical supercurrent I_C. A quantized conductance plateau at $2e^2/h$ corresponds to a single ballistic channel, and the associated I_C stays around 15 nA, which is smaller than the theoretical expectation[44] of $e\triangle/\hbar = 52$ nA ($\Delta \approx 215$ µeV). The discrepancy could be explained by intrinsic reasons though[45], to the best of our knowledge, the value I_C/Δ in our device is the largest for a single channel[46–49]. Unlike the STM or the break-junction experiments, where usually a mix of several channels contributes to the conductance[19,50], we demonstrate the single-channel limit unambiguously, beneficial for the investigation of the coherence. Figure 2b displays the conductance map at the weak-coupling regime, showing the peaks contributed by Cooper pairs, 2-charges (the 1st-order MARs), and single charges, as marked by the green, red, and blue triangles, respectively.

LZSM interference of single charges

We proceed to turn on the microwave and examine the LZSM interferometry. To verify our implementation of the interferometry, the JJ was first set to the tunneling limit at $V_G = -31$ V. Since the conductance scales roughly to $m\tau^m$, where τ is the transmission[51], the conductance peaks of multiple charges were heavily suppressed for small τ, leaving the single-charge coherence peaks as the prominent characteristics (Fig. 2b). Figure 2c depicts the dI/dV versus microwave power P and V_b at a frequency $f = 11.755$ GHz, exhibiting clear interference fringes consistent with Eq. (1). After considering an attenuation of the microwave and converting P to V_{RF}, the corresponding 2D FT is plotted in Fig. 2d, and the lemon-shaped ovals nicely follow the predictions of Eq. (2).

Figure 2e shows $\ln(W_{FT})$ as a function of k_ε, averaged near $k_A = 0$ to smooth out the singularities. Since $W_{FT} \propto e^{-\Gamma_2|k_\varepsilon|}$, a linear fit (red line) of the peak values (blue squares) generates a coherence time $T_2 = 0.075$ ns. In addition, the Lorentzian shape of Eq. (1) versus $\varepsilon = meV_0$ depends on T_2 as well. Figure 2f illustrates a Lorentzian fit (red curve) of the dI/dV versus $\Delta V_b = V_b - 2\Delta/e$ curve (black) at $P = -55$ dBm ($V_{RF} \approx 0$), which yields a similar $T_2 = 0.083$ ns.

Although T_2 is short, we demonstrate LZSM interferometry as a powerful approach to extract the coherence time of the charges in an open JJ. Two lower frequencies were further used, as shown in Fig. 2g, h for 7.665 GHz and Fig. 2i, j for 4.0 GHz. When the frequency decreases, the interference fringes become blurred because the time interval between two subsequent LZSM transitions increases and thus the interference loses coherence gradually[40]. The number of ovals in the Fourier space reveals a fingerprint of how many LZSM transitions (up to a factor of 2) can develop before decohering completely. Therefore, the observable ovals reduce from Fig. 2d to Fig. 2h, and to Fig. 2j. Please refer to Supplementary Note 5 for a detailed data analysis.

LZSM interference of various charges

The JJ was then configured to a slightly stronger coupled regime ($V_G = -28.9$ V) to release the tunneling of multiple charges and Cooper pairs. Figure 3a presents the interference fringes of the Cooper pairs, 2-charges through the 1st-order MARs and single charges, as marked by the square, circle, and triangle, respectively. The fringes of 3-charges through the 2nd-order MARs can also be recognized by the dashed lines in Fig. 3b, a zoom-in of Fig. 3a. The 2D FT maps were plotted in Fig. 3d–f, marked in correspondence with Fig. 3a, and their T_2 values were extracted as 0.1 ns, 0.049 ns, and 0.051 ns, for Cooper pairs, 2-charges, and single charges, respectively.

Taking the dI/dV versus V_b line-cut at $P = -45$ dBm in Fig. 3a as an input and using the T_2 values, the conductance map can be calculated. For this we assume that dI/dV is proportional to W and
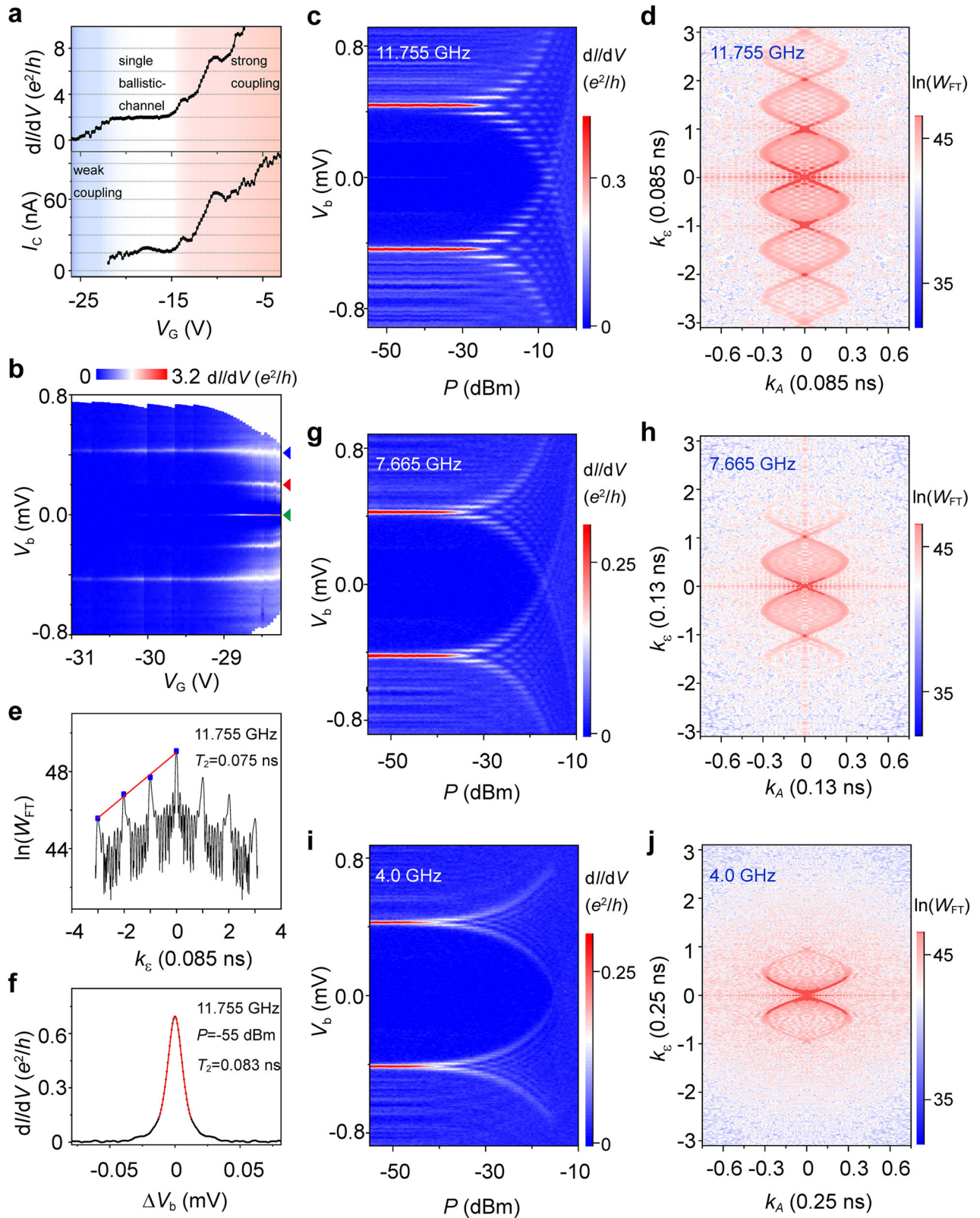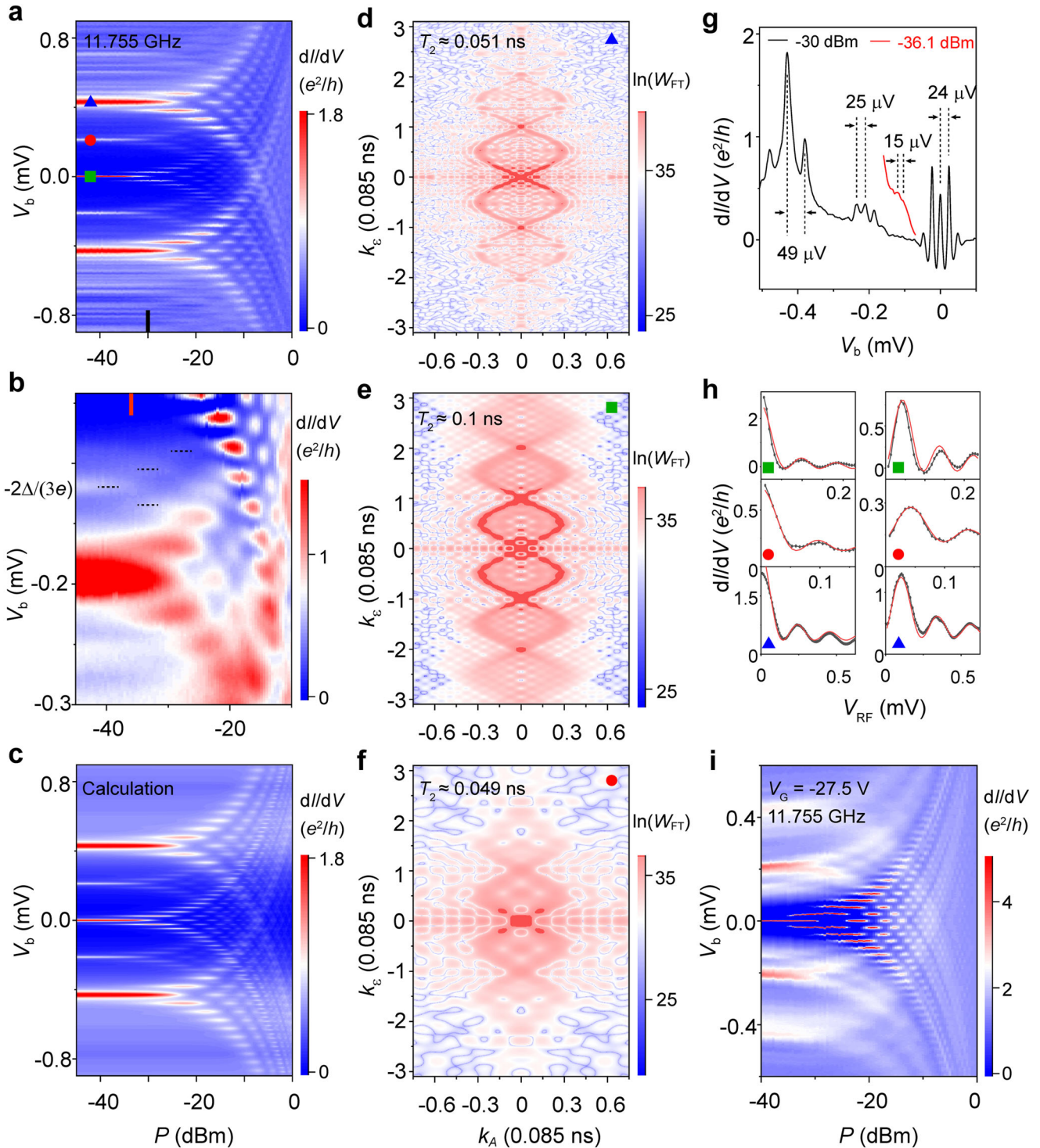
Fig. 2 LZSM interference of single charges in the tunneling limit. a Conductance dI/dV, measured in the normal state, and critical supercurrent I_c, both versus the gate voltage V_G. **b** dI/dV versus V_G and V_b at the weak coupling regime. The green, red and blue triangles mark the peaks of Cooper pairs, 2-charges of the 1st-order MARs, and single charges, respectively. **c** Interference fringes at $V_G = -31$ V and $f = 11.755$ GHz versus microwave power P and V_b. **d** The 2D FT of (**c**). For clarity, k_A and k_ε are in units of 1/f. **e** Averaged line-cut (black) near $k_A = 0$ of (**d**). The red line is a linear fit of the peak-values as marked by the blue squares. **f** Lorentzian fit (red curve) of the dI/dV data (black curve) versus $\Delta V_b = V_b - 2\Delta/e$ at $P = -55$ dBm of (**c**). The data for $\Delta V_b < 0$ are extracted from (**c**), and the $\Delta V_b > 0$ branch is simply mirrored. **g–j** Interference fringes and the corresponding 2D FT at $f = 7.665$ GHz (4.0 GHz).

its behavior follows Eq. (1). For example, if we consider the transport of single charges at $V_b = 2\Delta/e$, the number of electrons transferred from the left side to the right side of the JJ in unit time is W; i.e., the conductance is proportional to W. This is shown in Fig. 3c, which manifests a good agreement with the measured data in Fig. 3a. So far, we realized the measurement of the coherence times for the tunneling of various charges.

We next discuss about three more characteristics of the interference fringes. First, the number, m, of charges can be conveniently determined from the spacing δV_b of the satellite peaks,

Fig. 3 LZSM interference of various charges. a Interference fringes at $V_G = -28.9$ V and $f = 11.755$ GHz. The square, circle and triangle depict the contributions of Cooper pairs, 2-charges through the 1st-order MARs, and single charges, respectively. b Zoom-in of (a). The dashed lines highlight the features of 3-charges through the 2nd-order MARs. c, Calculated dI/dV based on both the dI/dV versus V_b curve at $P = -45$ dBm in (a) and the T_2 values shown in (d–f), which display the 2D FT maps of the sets of the fringes in (a). g Line-cuts taken from (a) and (b), as indicated by the black and red bars. h Extracted curves (black) from the fringes of (a) and the J_n^2 fit (red). The left column is for the $n = 0$ main peaks, and the right for the $n = 1$ satellite peaks. i Interference fringes at $V_G = -27.5$ V and $f = 11.755$ GHz.
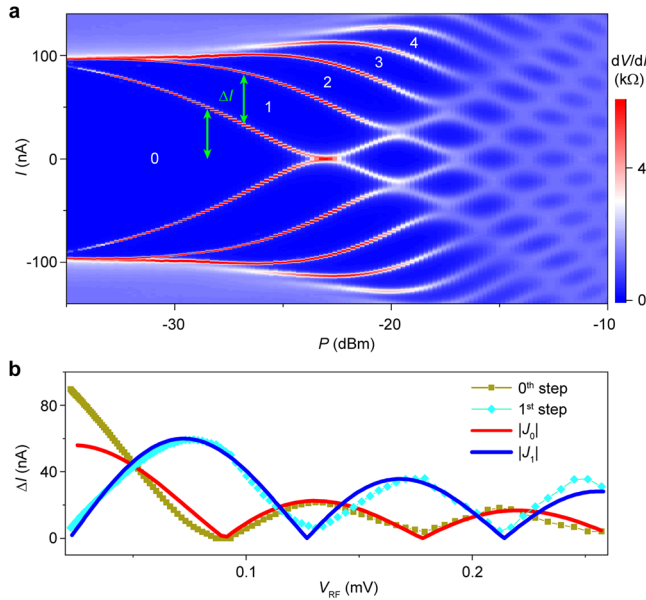
Fig. 4 Shapiro steps in the strong-coupling regime. a Differential resistance dV/dI versus P and current I, measured at $V_G = 6$ V and $f = 11.56$ GHz. The numbering indicates the Shapiro steps. **b** Step width ΔI versus V_{RF} and the corresponding Bessel function fitting to the 1st-order. A − 45 dB attenuation was assumed and subtracted.

since $\delta V_b \propto 1/m$. Figure 3g plots dI/dV versus the V_b curves taken from Fig. 3a, b, as indicated by the black and red bars. The spacings δV_b of 49 μV, 25 μV, 15 μV and 24 μV are consistent with charge numbers m of 1, 2, 3, and 2, at $V_b = -2\Delta/e$, $-2\Delta/(2e)$, $-2\Delta/(3e)$ and 0, respectively.

Second, the dI/dV peaks behave as J_n^2, versus the microwave amplitude V_{RF}. In Fig. 3h, the left and right columns show the extracted curves (black) from Fig. 3a for the main peak ($n = 0$) and the first satellite peak ($n = 1$), respectively. A good agreement was achieved by a J_n^2 fitting, from Eq. (1), as shown by the red curves. Note that a dI/dV constant was included in each fitting to account for the background conductance, and the power P has been converted to V_{RF}. Moreover, the J_n^2 dependence serves as evidence for Cooper-pair tunneling as microscopic particles near $V_b = 0$, instead of the macroscopic Shapiro-step picture whose characteristic width would rather follow J_n to the 1st-order[13,19], as shown below.

Onset and loss of the macroscopic coherence
Third, there is an opposite trend of the coherence for the Cooper pairs and the other charges (quasiparticles) when the coupling strength of the JJ increases. A clue can be found by examining the T_2 extracted above. When increasing the coupling strength of the JJ from $V_G = -31$ V to -28.9 V, T_2 for single charges drops from 0.075 ns to 0.051 ns. At $V_G = -28.9$ V, $T_2 = 0.049$ ns and 0.1 ns for 2-charges through MARs, and Cooper pairs, respectively.

When the coupling strength increases further, as shown in Fig. 3i at $V_G = -27.5$ V, the fringes for the Cooper pairs become more evident while the others fade away. This is consistent with the scenario that when the Josephson coupling and the related capacitance increase, the Cooper pairs tend to recover the macroscopic quantum coherence, but the quasiparticles decohere faster due to the energy broadening and the background conductance, etc.

Eventually, at the strong-coupling regime the macroscopic quantum coherence was fully restored and regular Shapiro steps were obtained at $V_G = 6$ V, and a good agreement was achieved by fitting the step width to the 1st-order of the Bessel function, $|J_n|$, as shown in Fig. 4.

We now comment on the advantages and drawbacks of the application of the LZSM model to Josephson junctions. (1) Advantages: as explained above, the LZSM model allows considering the tunneling of various charges from a different, but complementary, perspective; compared to the well-established microscopic theories. The involvement of coherence and decoherence is enabled in the quantum interference process. We can extract the coherence time of these various charges by the Fourier transform of the interference fringes and the Lorentzian fitting. It effectively includes the influence of various decoherence sources, such as tunnel coupling, thermal broadening, noise, etc. (2) Drawbacks: as we pointed out earlier, we treated the BCS singularity of the density of states as a δ-function; that is, the superconducting gap edge was modeled as a single level, and the continuous density of states outside the superconducting gap was omitted. The dependence of the coupling strength on bias voltage was also not taken into account. This leads to the missing of the background conductance curve which was studied in analytical microscopic theories. The LZSM model only focused on the conductance peaks and their evolution under microwaves to study the interference effect and the coherence/decoherence. As such, we restricted the analysis of the measured data inside the gap.

Conclusions
We realized the measurement of the coherence time of various charge states that tunnel back and forth in a JJ by implementing LZSM interferometry. Then, we revealed the change of the Cooper pairs in the JJ, from a macroscopic quantum coherent state to individual particle states; or conversely, the onset of macroscopic quantum coherence. We expect that the LZSM interferometry is a powerful technique for exploring the coherence time of charges tunneling in various hybrid devices, such as through trivial Andreev and Yu-Shiba-Rusinov bound sates[20], Floquet states[52], as well as topological Majorana bound states[53–56]. Note that these states might also be subjected to the crossover of the Cooper pairs from a macroscopic quantum coherence state to individual particle states.

METHODS
InAs$_{0.92}$Sb$_{0.08}$-Al nanowire growth
InAs$_{0.92}$Sb$_{0.08}$ nanowires were grown in a solid source molecular beam epitaxy system (VG V80H) on p-Si (111) substrates using Ag as catalysts[57]. The nanowires were grown for 40 min at a temperature of 465 °C with the beam fluxes of In, As and Sb sources of 1.1×10^{-7} mbar, 4.6×10^{-6} mbar and 4.7×10^{-7} mbar, respectively. After the growth of InAs$_{0.92}$Sb$_{0.08}$ nanowires, the sample was transferred from the growth chamber to the preparation chamber at 300 °C to avoid arsenic condensation on the nanowire surface. The sample was then cooled down to a low temperature (~−30 °C) by natural cooling and liquid nitrogen cooling[58]. Al was evaporated from a Knudsen cell at an angle of ~20° from the substrate normal (~70° from the substrate surface) and at a temperature of ~1150 °C for 180 s (giving ~0.08 nm/s). During the Al growth, the substrate rotation was kept disabled. When the growth of nanowires with Al was completed, the sample was rapidly pulled out of the MBE growth chamber and oxidized naturally.

Fabrication of the devices
The as-grown nanowires were transferred onto Si/SiO$_2$ (300 nm) substrates simply by a tissue. Standard electron-beam lithography was applied to fabricate the Ti/Au (10 nm/80 nm) electrodes using electron-beam evaporation. Note that an ion source cleaning and a soft plasma cleaning were performed to improve the contact prior to the deposition.

Transport measurements

The measurements were carried out in a cryo-free dilution refrigerator at a base temperature of ~10 mK. Low-frequency lock-in techniques were utilized to measure the conductance of the JJ, $dI/dV \equiv I_{ac}/V_{ac}$, with a small excitation ac voltage V_{ac} and a dc bias voltage V_b applied and the ac current I_{ac} measured. The microwave driving was supplied through a semi-rigid coaxial cable with an open end which is several millimeters above the JJ, serving as an antenna.

Data analysis

The measured LZSM interference for the various charges in our small JJ manifests as sets of dI/dV fringes as a function of microwave power P and bias voltage V_b. However, P is the output of the signal generator, and the effective power P_{eff} on the JJ needs to be determined. To do so, we calculated the interference fringes for a given measured data set using Eq. (1), and compare their power difference of the $n = 0$ peaks to extract the attenuation of the microwave, i.e., $P–P_{eff}$. Afterwards, the measured interference fringes were selected and converted from power (P_{eff}) dependence to amplitude (V_{RF}) dependence. And the data set was further symmetrized to the four quadrants and scaled to a maximum of 1 to carry out the 2D FT. A detailed interpretation can be found in the Supplementary Note 5.

DATA AVAILABILITY

The data supporting the findings of this study are available from the corresponding authors upon reasonable request.

CODE AVAILABILITY

The code supporting the findings of this study are available from the corresponding authors upon reasonable request.

REFERENCES

1. Winful, H. G. Tunneling time, the Hartman effect, and superluminality: a proposed resolution of an old paradox. *Phys. Rep.* **436**, 1–69 (2006).
2. Landsman, A. S. & Keller, U. Attosecond science and the tunnelling time problem. *Phys. Rep.* **547**, 1–24 (2015).
3. Niu, Q. & Raizen, M. G. How Landau-Zener tunneling takes time. *Phys. Rev. Lett.* **80**, 3491–3494 (1998).
4. Niu, Q., Zhao, X. G., Georgakis, G. A. & Raizen, M. G. Atomic Landau-Zener tunneling and Wannier-Stark ladders in optical potentials. *Phys. Rev. Lett.* **76**, 4504–4507 (1996).
5. Sainadh, U. S. et al. Attosecond angular streaking and tunnelling time in atomic hydrogen. *Nature* **568**, 75–77 (2019).
6. Ramos, R., Spierings, D., Racicot, I. & Steinberg, A. M. Measurement of the time spent by a tunnelling atom within the barrier region. *Nature* **583**, 529–532 (2020).
7. Streltsov, A., Adesso, G. & Plenio, M. B. Colloquium: quantum coherence as a resource. *Rev. Mod. Phys.* **89**, 041003 (2017).
8. Klapwijk, T. M., Blonder, G. E. & Tinkham, M. Explanation of subharmonic energy gap structure in superconducting contacts. *Phys. B+C.* **109-110**, 1657–1664 (1982).
9. Falci, G., Bubanja, V. & Schön, G. Quasiparticle and Cooper pair tunneling in small capacitance Josephson junctions. *Z. Phys. B - Condens. Matter* **85**, 451–458 (1991).
10. Octavio, M., Tinkham, M., Blonder, G. E. & Klapwijk, T. M. Subharmonic energy-gap structure in superconducting constrictions. *Phys. Rev. B* **27**, 6739–6746 (1983).
11. Ridderbos, J. et al. Multiple Andreev reflections and Shapiro steps in a Ge-Si nanowire Josephson junction. *Phys. Rev. Mater.* **3**, 084803 (2019).
12. Tinkham, M. *Introduction to Superconductivity*. (McGraw-Hill, Inc., New York, 1996).
13. Roychowdhury, A., Dreyer, M., Anderson, J. R., Lobb, C. J. & Wellstood, F. C. Microwave photon-assisted incoherent cooper-pair tunneling in a Josephson STM. *Phys. Rev. Appl.* **4**, 034011 (2015).
14. Shapiro, S. Josephson currents in superconducting tunneling: the effect of microwaves and other observations. *Phys. Rev. Lett.* **11**, 80–82 (1963).
15. Boris, A. A. & Krasnov, V. M. Quantization of the superconducting energy gap in an intense microwave field. *Phys. Rev. B* **92**, 174506 (2015).
16. Shaikhaidarov, R. S. et al. Quantized current steps due to the a.c. coherent quantum phase-slip effect. *Nature* **608**, 45–49 (2022).
17. Tien, P. K. & Gordon, J. P. Multiphoton process observed in the interaction of microwave fields with the tunneling between superconductor films. *Phys. Rev.* **129**, 647–651 (1963).
18. Cuevas, J. C., Heurich, J., Martín-Rodero, A., Levy Yeyati, A. & Schön, G. Sub-harmonic Shapiro steps and assisted tunneling in superconducting point contacts. *Phys. Rev. Lett.* **88**, 157001 (2002).
19. Kot, P. et al. Microwave-assisted tunneling and interference effects in super-conducting junctions under fast driving signals. *Phys. Rev. B* **101**, 134507 (2020).
20. Peters, O. et al. Resonant Andreev reflections probed by photon-assisted tunnelling at the atomic scale. *Nat. Phys.* **16**, 1222–1226 (2020).
21. González, S. A. et al. Photon-assisted resonant Andreev reflections: Yu-Shiba-Rusinov and Majorana states. *Phys. Rev. B* **102**, 045413 (2020).
22. Shevchenko, S. N., Ashhab, S. & Nori, F. Landau–Zener–Stückelberg interferometry. *Phys. Rep.* **492**, 1–30 (2010).
23. Ivakhnenko, O. V., Shevchenko, S. N. & Nori, F. Nonadiabatic Landau–Zener–Stückelberg–Majorana transitions, dynamics, and interference. *Phys. Rep.* **995**, 1–89 (2023).
24. Shevchenko, S. N. *Mesoscopic Physics Meets Quantum Engineering*. (World Scientific, 2019).
25. Oliver, W. D. et al. Mach-Zehnder interferometry in a strongly driven super-conducting qubit. *Science* **310**, 1653 (2005).
26. Berns, D. M. et al. Amplitude spectroscopy of a solid-state artificial atom. *Nature* **455**, 51–57 (2008).
27. Stehlik, J. et al. Landau-Zener-Stückelberg interferometry of a single electron charge qubit. *Phys. Rev. B* **86**, 121303 (2012).
28. Petta, J. R., Lu, H. & Gossard, A. C. A coherent beam splitter for electronic spin states. *Science* **327**, 669–672 (2010).
29. Wang, Z., Huang, W.-C., Liang, Q.-F. & Hu, X. Landau-Zener-Stückelberg Inter-ferometry for Majorana Qubit. *Sci. Rep.* **8**, 7920 (2018).
30. Kervinen, M., Ramírez-Muñoz, J. E., Välimaa, A. & Sillanpää, M. A. Landau-Zener-Stückelberg interference in a multimode electromechanical system in the quantum regime. *Phys. Rev. Lett.* **123**, 240401 (2019).
31. Bogan, A. et al. Landau-Zener-Stückelberg-Majorana interferometry of a single hole. *Phys. Rev. Lett.* **120**, 207701 (2018).
32. Koski, J. V. et al. Floquet spectroscopy of a strongly driven quantum dot charge qubit with a microwave resonator. *Phys. Rev. Lett.* **121**, 043603 (2018).
33. Larkin, A. I. & Ovchinnikov, Y. N. Tunnel effect between superconductors in an alternating field. *Sov. Phys. JETP* **24**, 1305 (1967).
34. Barone, A. & Paternò, G. *Physics and Applications of the Josephson Effect*. (John Wiley & Sons, Inc., 1982).
35. Martinis, J. M., Devoret, M. H. & Clarke, J. Experimental tests for the quantum behavior of a macroscopic degree of freedom: the phase difference across a Josephson junction. *Phys. Rev. B* **35**, 4682–4698 (1987).
36. Koval, Y., Fistul, M. V. & Ustinov, A. V. Enhancement of Josephson phase diffusion by microwaves. *Phys. Rev. Lett.* **93**, 087004 (2004).
37. Yu, H. F. et al. Quantum phase diffusion in a small underdamped Josephson junction. *Phys. Rev. Lett.* **107**, 067004 (2011).
38. Carrad, D. J. et al. Photon-assisted tunneling of high-order multiple andreev reflections in epitaxial nanowire Josephson junctions. *Nano Lett.* **22**, 6262–6267 (2022).
39. Gorelik, L. Y., Lundin, N. I., Shumeiko, V. S., Shekhter, R. I. & Jonson, M. Super-conducting single-mode contact as a microwave-activated quantum inter-ferometer. *Phys. Rev. Lett.* **81**, 2538–2541 (1998).
40. Rudner, M. S. et al. Quantum phase tomography of a strongly driven qubit. *Phys. Rev. Lett.* **101**, 190502 (2008).
41. Berns, D. M. et al. Coherent quasiclassical dynamics of a persistent current qubit. *Phys. Rev. Lett.* **97**, 150502 (2006).
42. Krogstrup, P. et al. Epitaxy of semiconductor–superconductor nanowires. *Nat. Mater.* **14**, 400–406 (2015).
43. Chang, W. et al. Hard gap in epitaxial semiconductor-superconductor nanowires. *Nat. Nanotechnol.* **10**, 232–236 (2015).
44. Beenakker, C. W. J. & van Houten, H. Josephson current through a super-conducting quantum point contact shorter than the coherence length. *Phys. Rev. Lett.* **66**, 3056–3059 (1991).
45. Nikolić, B. K., Freericks, J. K. & Miller, P. Intrinsic reduction of Josephson critical current in short ballistic SNS weak links. *Phys. Rev. B* **64**, 212507 (2001).
46. Xiang, J., Vidan, A., Tinkham, M., Westervelt, R. M. & Lieber, C. M. Ge/Si nanowire mesoscopic Josephson junctions. *Nat. Nanotechnol.* **1**, 208–213 (2006).

47. Irie, H., Harada, Y., Sugiyama, H. & Akazaki, T. Josephson coupling through one-dimensional ballistic channel in semiconductor-superconductor hybrid quantum point contacts. *Phys. Rev. B* **89**, 165415 (2014).

48. Abay, S. et al. Quantized conductance and its correlation to the supercurrent in a nanowire connected to superconductors. *Nano Lett.* **13**, 3614–3617 (2013).

49. Hendrickx, N. W. et al. Ballistic supercurrent discretization and micrometer-long Josephson coupling in germanium. *Phys. Rev. B* **99**, 075435 (2019).

50. Chauvin, M. et al. Superconducting atomic contacts under microwave irradiation. *Phys. Rev. Lett.* **97**, 067006 (2006).

51. Kjaergaard, M. et al. Transparent semiconductor-superconductor interface and induced gap in an epitaxial heterostructure Josephson junction. *Phys. Rev. Appl.* **7**, 034029 (2017).

52. Park, S. et al. Steady Floquet–Andreev states in graphene Josephson junctions. *Nature* **603**, 421–426 (2022).

53. van Zanten, D. M. T. et al. Photon-assisted tunnelling of zero modes in a Majorana wire. *Nat. Phys.* **16**, 663–668 (2020).

54. Mourik, V. et al. Signatures of Majorana fermions in hybrid superconductor-semiconductor nanowire devices. *Science* **336**, 1003–1007 (2012).

55. Prada, E. et al. From Andreev to Majorana bound states in hybrid superconductor–semiconductor nanowires. *Nat. Rev. Phys.* **2**, 575–594 (2020).

56. Zhang, P. et al. Missing odd-order Shapiro steps do not uniquely indicate fractional Josephson effect. Preprint at https://arxiv.org/abs/2211.08710 (2022).

57. Wen, L. et al. Large-composition-range pure-phase homogeneous $InAs_{1-x}Sb_x$ nanowires. *J. Phys. Chem. Lett.* **13**, 598–605 (2022).

58. Pan, D. et al. In situ epitaxy of pure phase ultra-thin InAs-Al nanowires for quantum devices. *Chin. Phys. Lett.* **39**, 058101 (2022).

ACKNOWLEDGEMENTS

AUTHOR CONTRIBUTIONS

F.Q. conceived and supervised the project. D.P. grew and characterized the nanowires. J.Z. supervised the nanowire growth. J.H. and M.L. fabricated the devices and performed the transport measurements. Z.L., Z.J., G.Y., S.Z., G.L., J.S., L.L. and F.Q. supported the fabrication and measurements. J.H. and F.Q. analyzed the data with the help of Z.L., G.Y., S.N.S. and F.N. F.Q., J.H., D.P., L.L., S.N.S., and F.N. wrote the manuscript, with input from all authors.

COMPETING INTERESTS

The authors declare no competing interests.

ADDITIONAL INFORMATION

Supplementary information The online version contains supplementary material available at https://doi.org/10.1038/s41534-023-00798-2.

Correspondence and requests for materials should be addressed to Franco Nori, Jianhua Zhao, Li Lu or Fanming Qu.

Reprints and permission information is available at http://www.nature.com/reprints

Publisher's note Springer Nature remains neutral with regard to jurisdictional claims in published maps and institutional affiliations.